crystals

MDPI

Article

Combination Synthesis of NbB_2–Spinel $MgAl_2O_4$ Composites from MgO-Added Thermite-Based Reactants with Excess Boron

Chun-Liang Yeh * and Yin-Chien Chen

Department of Aerospace and Systems Engineering, Feng Chia University, Taichung 40724, Taiwan; m0626603@fcu.edu.tw

* Correspondence: clyeh@fcu.edu.tw; Tel.: +886-4-2451-7250 (ext. 3963)

Received: 24 February 2020; Accepted: 17 March 2020; Published: 18 March 2020

Abstract: The formation of NbB_2–$MgAl_2O_4$ composites from the MgO-added thermite-based reaction systems was investigated by self-propagating high-temperature synthesis (SHS). Two thermite mixtures, $Nb_2O_5/B_2O_3/Al$ and Nb_2O_5/Al, were, respectively, adopted in Reactions (1) and (2). The XRD analysis confirmed the combination of Al_2O_3 with MgO to form $MgAl_2O_4$ during the SHS process and that excess boron of 30 atom.% was required to yield NbB_2–$MgAl_2O_4$ composites with negligible NbB and Nb_3B_4. The microstructure of the composite reveals that rod-shaped $MgAl_2O_4$ crystals are closely interlocked and granular NbB_2 are embedded in or scattered over $MgAl_2O_4$. With the addition of $MgAl_2O_4$, the fracture toughness (K_{IC}) of 4.37–4.82 MPa $m^{1/2}$ was obtained for the composites. The activation energies E_a = 219.5 ± 16 and 167.9 ± 13 kJ/mol for Reactions (1) and (2) were determined from combustion wave kinetics.

Keywords: boride NbB_2; spinel $MgAl_2O_4$; combustion synthesis; microstructure; thermite

1. Introduction

Transition metal (IVB and VB) diborides, such as TiB_2, ZrB_2, NbB_2, and TaB_2, have been referred to as ultra-high-temperature ceramics (UHTCs). Transition metal diborides crystallize in the hexagonal $A1B_2$ type structure (space group P6/mmm) with *c*/*a* ratio close to unity. In this arrangement, the hexagonal nets of metal atoms and triangle nets of pure boron atoms are alternately stacked along the *c* axis [1]. Besides their melting points exceeding 3000 °C, they possess a unique combination of high hardness, thermal conductivity, electrical conductivity, excellent chemical stability, corrosion resistance, and thermal shock resistance [2–5]. They have found a broad range of applications in the mechanical, automobile, aerospace industries, etc. [5]. To improve the refractory properties of metal borides and carbides, Al_2O_3 or $MgAl_2O_4$ (magnesium aluminate spinel) has been considered as an additive. Extensive studies have been conducted on understanding the production and characteristics of different metal borides reinforced by Al_2O_3 [6–10], but relatively few studies have focused on the boride–$MgAl_2O_4$ composite [11].

$MgAl_2O_4$ is of particular interest due to its exceptional mechanical, thermal, and optical properties, such as high melting point (2135 °C), high hardness (16 GPa), relatively low density (3.58 g/cm^3), high mechanical strength (135–216 MPa), good transmittance in the wavelength range of 0.25 to 5.0 μm, high thermal shock resistance, high chemical inertness, low dielectric constant, and low thermal expansion coefficient [12,13]. $MgAl_2O_4$ spinel has a close-packed face-centered cubic (fcc) structure of space group *Fd3m* (number 227). There are eight $MgAl_2O_4$ units per cubic cell. Mg and Al cations occupy 1/8 of the tetrahedral sites and 1/2 of the octahedral sites and there are 32 oxygen ions in the unit cell. In the normal spinel, all Al^{3+} ions are in octahedral coordination with local symmetry D_{3d}

and all Mg^{2+} ions are in tetrahedral coordination with point group symmetry T_d. The anion sublattice is arranged in a pseudo-cubic close-packed (ccp) spatial configuration. There are four layers of AlO_6 octahedral chains along the *c* axis in one unit cell [12]. Fabrication of $MgAl_2O_4$ and other spinel compounds like $NiFe_2O_4$ and $CoFe_2O_4$ by either solid-state or wet-chemistry reaction methods usually requires long processing time and complicated steps [14–18].

With the merits of energy and time savings, simple operation, and high-purity products, combustion synthesis in the mode of self-propagating high-temperature synthesis (SHS) has been recognized as an alternative route to material synthesis and processing [19,20]. When the SHS process is combined with the aluminothermic or magnesiothermic reduction of metal oxides to generate Al_2O_3 or MgO, the multistage combustion reaction represents an in situ approach to producing $MgAl_2O_4$-containing composites [21–25]. Horvitz and Gotman [21] obtained TiAl–Ti_3Al–$MgAl_2O_4$ composites from the powder compacts composed of $2TiO_2$–Mg–4Al via the SHS reaction and thermal explosion. Magnesiothermic reduction of WO_3 and B_2O_3 in the presence of Al_2O_3 under the SHS manner was conducted by Omran et al. [22] to prepare $MgAl_2O_4$–W and $MgAl_2O_4$–W–W_2B composites. With the use of MoO_3, SiO_2, and Al as the thermite reagents mixing with Mo, Si, and MgO powders for the SHS reaction, the formation of various molybdenum silicides ($MoSi_2$, Mo_5Si_3, and Mo_3Si) and $MgAl_2O_4$ composites was achieved [23–25].

This study made an attempt to investigate the preparation of NbB_2–$MgAl_2O_4$ in situ composites via a reduction-based SHS process. The multistage combustion process involves the aluminothermic reduction of Nb_2O_5 and B_2O_3 in the presence of MgO, elemental interaction of Nb with B, and the combination of MgO with Al_2O_3. To resolve the loss of boron in the form of gas-phase B_2O_2 and BO during the SHS process [8,9], this study examined test specimens with excess boron. The effects of thermite reagents and excess boron on the reaction exothermicity and combustion wave kinetics were explored. Moreover, the phase composition, microstructure, and mechanical properties of the final products were characterized.

2. Materials and Methods

The starting materials utilized by this study included niobium (V) oxide (Nb_2O_5) (Strem Chemicals, <45 μm, 99.9%, Newburyport, MA, US), B_2O_3 (Strem Chemicals, 99.9%), Al (Showa Chemical Co., <45 μm, 99.9%, Tokyo, Japan), Nb (Strem Chemicals, <45 μm, 99.8%), amorphous boron (Noah Technologies Corp., <1 μm, 92%, San Antonio, TX, US), and MgO (Alfa Aesar, 99%, Ward Hill, MA, US). Two MgO-added combustion systems with different thermite reagents were studied. As expressed below, Reaction (1) comprises Nb_2O_5 and B_2O_3 as thermite oxidants, while Reaction (2) has Nb_2O_5 only. For both reaction systems, Al acts as the thermite reductant.

$$\left[\frac{x}{2}Nb_2O_5 + \left(1 - \frac{5}{6}x\right)B_2O_3 + 2Al\right] + \left(\frac{11}{3}x - 2\right)B + MgO \rightarrow xNbB_2 + MgAl_2O_4 \quad \text{(R1)}$$

$$\left(\frac{3}{5}Nb_2O_5 + 2Al\right) + \left(y - \frac{6}{5}\right)Nb + 2yB + MgO \rightarrow yNbB_2 + MgAl_2O_4 \quad \text{(R2)}$$

where *x* and *y* are stoichiometric coefficients signifying the mole number of NbB_2 formed per unit mole of $MgAl_2O_4$ in Reactions (1) and (2), respectively.

The experiments of Reaction (1) were performed with x = 0.6–1.0. The increase of *x* raises the amount of Nb_2O_5 but reduces that of B_2O_3 in the reactant mixture. Under this condition, more amorphous boron is added to make up for the decrease of boron provided from B_2O_3. Samples of Reaction (2) were formulated with y = 1.2–1.8. The increase of *y* augments elemental Nb and B for the production of a larger amount of NbB_2, but has no change in the molar quantity of thermite reagents, Nb_2O_5 and Al, in Reaction (2). A combination of Reactions (1) and (2) renders this study feasible to obtain products with a molar proportion of $NbB_2/MgAl_2O_4$ from 0.6 to 1.8. In addition, the SHS reactions with test specimens containing excess boron of 20 and 30 atom.% were conducted to examine the extent of boron loss during combustion and to compensate for the relatively low purity (92%) of

amorphous boron used in this study. It should be noted that boron has high hardness, great stability in extreme environments, and good resistance to heat. It has several forms, the most common of which is amorphous boron, and is unreactive to oxygen, water, acids, and alkalis. While barely reactive at room temperature, boron reacts strongly at high temperature with metals to form borides. Moreover, its reducing properties allow it to react with numerous compounds and, as in the case of oxygenated or halogenated compounds, in a violent manner [26].

In Reaction (1), the aluminothermic reduction of Nb_2O_5 (the reaction enthalpy, ΔH_r = −536 kJ/mol of Al_2O_3 and the adiabatic temperature, T_{ad} = 2756 K) is more energetic than that of B_2O_3 (ΔH_r = −403.8 kJ/mol of Al_2O_3 and T_{ad} = 2315 K) [27,28]. The intermetallic reaction of Nb + 2B to yield NbB_2 with formation enthalpy ΔH_f = −175.3 kJ/mol and T_{ad} = 2315 K is exothermically comparable to the B_2O_3 + 2Al reaction [29]. The combination reaction between MgO and Al_2O_3 to form $MgAl_2O_4$ is weakly exothermic with ΔH_r = −35.6 kJ [23]. This means that with the increase of NbB_2 content (the x value), two opposing effects govern the combustion exothermicity of Reaction (1). As far as Reaction (2) is concerned, the increase of y for the formation of a larger NbB_2 content has a dilution effect on combustion. To elucidate the combustion exothermicity, calculation of T_{ad} of Reactions (1) and (2) under different stoichiometric coefficients was performed according to the following equation [23,30] with thermochemical data taken from [29].

$$\Delta H_r + \int_{298}^{T_{ad}} \sum n_j C_p\left(P_j\right) dT + \sum_{298-T_{ad}} n_j L\left(P_j\right) = 0$$

where ΔH_r is the reaction enthalpy at 298 K, n_j is the stoichiometric constant, C_p and L are the heat capacity and latent heat, and P_j refers to the product. Calculations of the adiabatic temperature were based upon the final products of stoichiometric reactions described in R(1) and R(2).

Reactant powders were mixed in a ball mill and then uniaxially compressed in a stainless-steel mold at a pressure of 70–80 MPa to form cylindrical test samples with 7 mm in diameter, 12 mm in height, and a relative density of 60%. The relative density of the test specimen is related to the initial components. The theoretical density (ρ_{TD}) of the test specimen is calculated from the mass fraction (Y) and density (ρ) of each component through the following equation.

$$\frac{1}{\rho_{TD}} = \frac{Y_{Nb2O5}}{\rho_{Nb2O5}} + \frac{Y_{B2O3}}{\rho_{B2O3}} + \frac{Y_{Al}}{\rho_{Al}} + \frac{Y_B}{\rho_B} + \frac{Y_{MgO}}{\rho_{MgO}}$$

The SHS experiments were conducted in a windowed combustion chamber filled with high-purity (99.99%) argon. The propagation velocity of the combustion wave (V_f) was determined from the time sequence of recorded pictures. The reaction temperature was measured by the Pt/Pt-13%Rh bare wire thermocouple with a bead diameter of 125 μm. A thin ceramic (SiO_2) coating is usually to prevent the catalytic effect on the thermocouple in the measurement of gas-phase flame temperature of a combustion mixture involving hydrogen, methane, or propane as the fuel. Because solid-state combustion with argon as the surrounding gas is under investigation, the thermocouple without an inert coating was used by this work. Details of the experimental setup and scheme were described elsewhere [25,31]. After the SHS process, phase constituents of the products were analyzed by an X-ray diffractometer (Bruker D2, Billerica, MA, US) using CuK_α radiation. The microstructure of the final product was examined by a scanning electron microscope (Hitachi S3000H, Tokyo, Japan) and elemental proportion was deduced from the energy dispersive spectroscopy (EDS). For Vickers hardness (H_v) and fracture toughness (K_{IC}) measurement, selected experiments with the reactant compact placing in a steel mold were conducted. Upon the completion of the self-sustaining combustion reaction, densification of the product was carried out by a hydraulic press machine [25].

3. Results and Discussion

3.1. Combustion Wave Kinetics and Reaction Temperature

Figure 1 illustrates a typical series of combustion images obtained by this study, which was recorded from the powder compact of Reaction (2) with $y = 1.4$. As can be seen in Figure 1, a well-defined combustion wave is established upon ignition and propagates throughout the entire sample in a self-sustaining manner. This demonstrates sufficient reaction exothermicity of the reactant mixture. After combustion, the burned sample essentially retained its original shape.

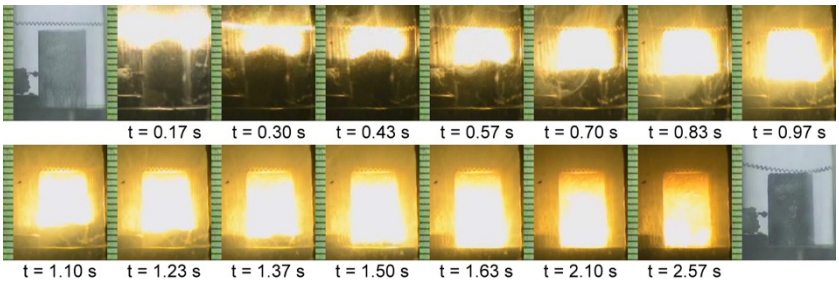

Figure 1. Typical sequence of self-sustaining combustion images recorded from Reaction (2) with $y = 1.4$.

The influence of the stoichiometric coefficient and excess boron on the flame-front velocity of Reactions (1) and (2) is presented in Figure 2. It was found that for the samples without excess boron, the combustion wave velocity of Reaction (1) increased from 2.5 to 6.6 mm/s with x increasing from 0.6 to 1.0, while that of Reaction (2) decreased from 8.4 to 4.8 mm/s with y in the range from 1.2 to 1.8. To be presented lately, it is believed that the variation of combustion front velocity with the reaction stoichiometry depends mainly on the exothermicity of the SHS process. As also indicated in Figure 2, samples with excess boron of 30 atom.% exhibit lower combustion wave speeds when compared to those without additional boron. This could be attributable to a prolonged sequence of phase evolution of borides in response to the increase of boron.

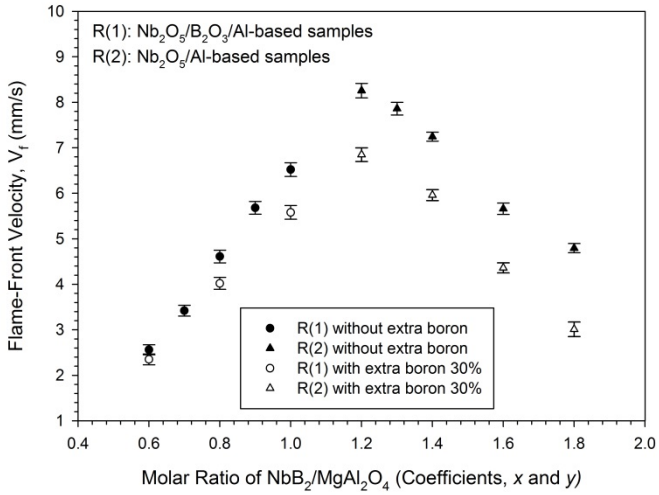

Figure 2. Effects of $NbB_2/MgAl_2O_4$ ratio and excess boron on flame-front propagation velocity of Reactions (1) and (2).

Figure 3 plots several measured sample temperature profiles, which depict a sharp rise signifying the rapid arrival of the combustion wave and a peak value corresponding to the combustion front temperature (T_c). After the progression of the combustion wave, a substantial temperature decline is a consequence of heat loss to the surroundings. As revealed in Figure 3, the peak temperature

(T_c = 1516 °C) of Reaction (1) with x = 0.9 is higher than that of x = 0.6 (T_c = 1317 °C) and the combustion front temperature of Reaction (2) decreases from 1606 °C to 1416 °C with an increase of y from 1.2 to 1.8. Based on the experimental measurement, the stoichiometric dependence of the combustion wave temperature is in agreement with that of flame-front velocity.

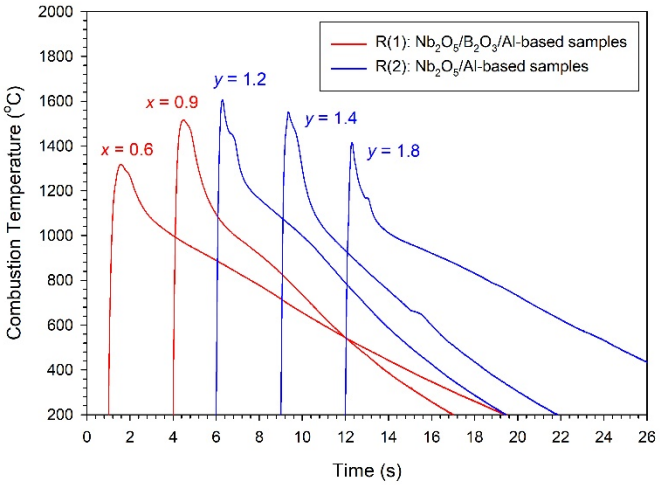

Figure 3. Combustion temperature profiles measured from samples of Reactions (1) and (2) with different stoichiometric coefficients.

A comparison between the calculated adiabatic temperature and measured combustion front temperature of Reactions (1) and (2) is presented in Figure 4, indicative of a consistent variation of T_{ad} and T_c with the reaction stoichiometry. The increase of the combustion temperature of Reaction (1) with increasing $NbB_2/MgAl_2O_3$ ratio is ascribed to a larger proportion of Nb_2O_5 to B_2O_3 in the thermite mixture, since the aluminothermic reduction of Nb_2O_5 is more exothermic. However, a decline of the combustion temperature of Reaction (2) with $NbB_2/MgAl_2O_3$ molar ratio confirms the cooling effect on combustion by increasing Nb and B, because the elemental reaction of Nb with B is less energetic than the thermite reaction of Nb_2O_5 and Al. As shown in Figure 4, the values of T_{ad} are higher by about 350–400 °C than those of T_c. The discrepancy between T_c and T_{ad} might result from considerable heat loss mostly by radiation, substantial boron elimination from the reaction zone, and formation of boride phases different from the stoichiometric composition.

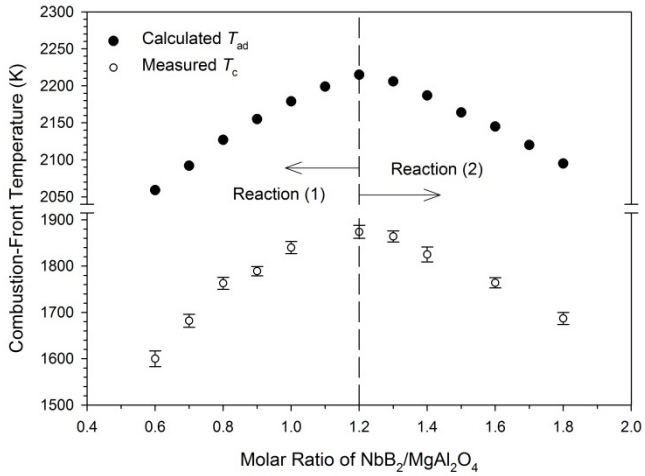

Figure 4. Calculated adiabatic temperatures and measured combustion temperatures of Reactions (1) and (2) as a function of the $NbB_2/MgAl_2O_4$ molar ratio.

The activation energy (E_a) of solid-state combustion was deduced from combustion wave kinetics by constructing a correlation between $\ln(V_f/T_c)^2$ and $1/T_c$ in a form of linear relationship [32,33]. Figure 5 depicts two sets of experimental data with best-fitted straight lines. From the slopes of straight lines, E_a = 219.5 ± 16 and 167.9 ± 13 kJ/mol were deduced for Reactions (1) and (2), respectively. A larger E_a for Reaction (1) means a higher kinetic barrier in comparison to Reaction (2). This could be caused most likely by the fact that the co-reduction of Nb_2O_5 and B_2O_3 by Al is required in Reaction (1) for the synthesis sequence to proceed, but Reaction (2) has only Nb_2O_5 to be reduced. According to Arrhenius kinetics, the activation energy of the solid-state reaction is governed by the reaction mechanism. In this study, aluminothermic reduction of metal oxides is considered as a first step of the SHS process, which is followed by a combination of Al_2O_3 and MgO to form $MgAl_2O_4$ and elemental interactions between Nb and B to produce NbB_2.

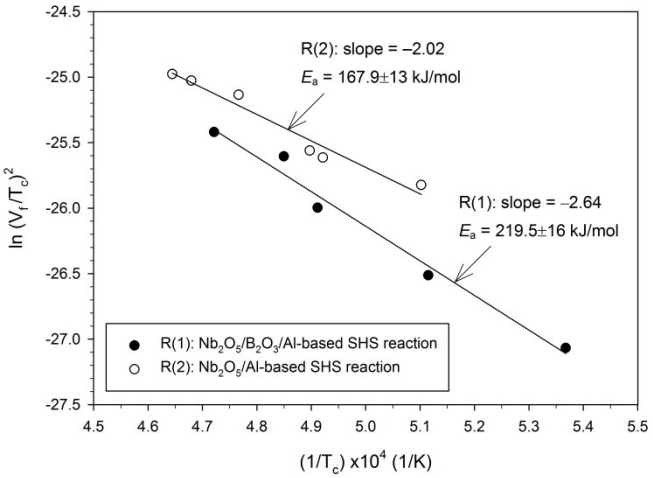

Figure 5. Correlation between combustion wave velocity and temperature for determination of activation energies (E_a) of Reactions (1) and (2).

3.2. Phase Composition and Microstructure of As-Synthesized Products

Figure 6a–c displays the XRD patterns of SHS-derived products from Reaction (1) of x = 1.0 without and with excess boron. As shown in Figure 6, $MgAl_2O_4$ is identified and niobium borides exist in three phases including NbB_2, Nb_3B_4, and NbB. The formation of $MgAl_2O_4$ confirms a combination reaction between pre-added MgO and thermite-produced Al_2O_3. The presence of NbB and Nb_3B_4 denotes that the amount of boron is inadequate to transform all the borides into NbB_2. For the sample without extra boron, as shown in Figure 6a, NbB is the dominant boride phase. Besides, there is NbO_2 detected in the final product, indicative of an incomplete reduction of Nb_2O_5. For the sample with excess boron of 20 atom.%, Figure 6b indicates that the yield of Nb_3B_4 and NbB_2 is enhanced and NbO_2 is no longer detectable. Furthermore, Figure 6c reveals that more NbB_2 is formed in the final product obtained from the sample with extra boron of 30 atom.%. Although NbB_2 is the dominant boride in Figure 6c, the other two borides, NbB and Nb_3B_4, are not trivial. This means a substantial boron loss from the samples of Reaction (1) possibly through two different paths. One is the reduction of B_2O_3 and the other is the borothermal reaction between Nb_2O_5 and boron. Both reactions could generate gaseous B_2O_2 and BO, and they might expel from the sample compact.

The effect of excess boron on the formation of borides for Reaction (2) is presented in Figure 7a–c. Likewise, excess boron enhanced the production of NbB_2. It was found that the improvement is more effective for Reaction (2) than Reaction (1). Figure 7b unveils that NbB_2 prevails over NbB and Nb_3B_4 for the sample with excess boron of 20 atom.%. Moreover, as shown in Figure 7c, NbB and Nb_3B_4 become negligible in the resulting product from the sample with excess boron of 30 atom.%. This is because Reaction (2) contains no B_2O_3, only borothermal reduction of Nb_2O_5 could result in the loss of boron.

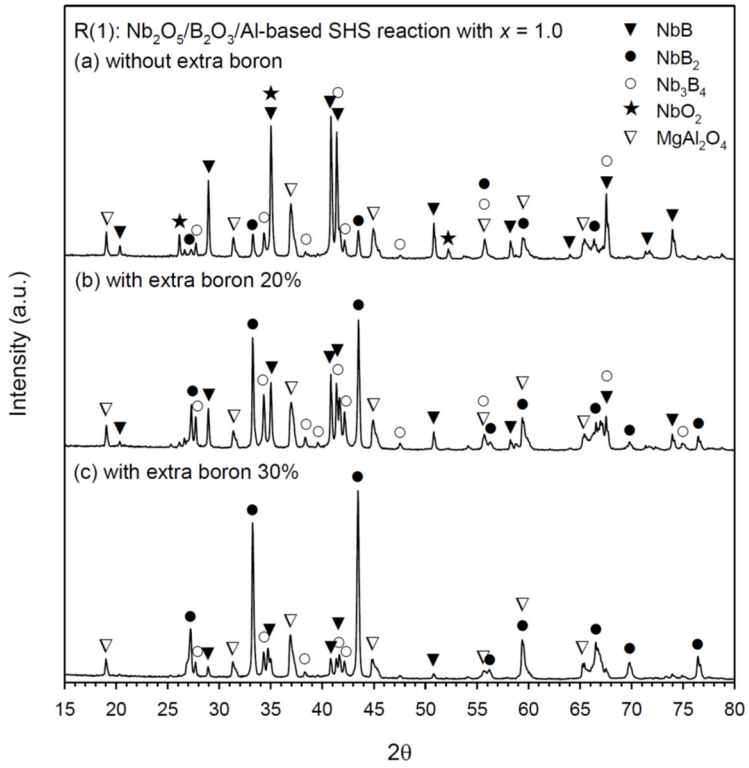

Figure 6. XRD patterns of NbB_2–$MgAl_2O_4$ composites synthesized from Reaction (1) of x = 1.0 under conditions: (**a**) without extra boron, (**b**) with extra boron 20%, and (**c**) with extra boron 30%.

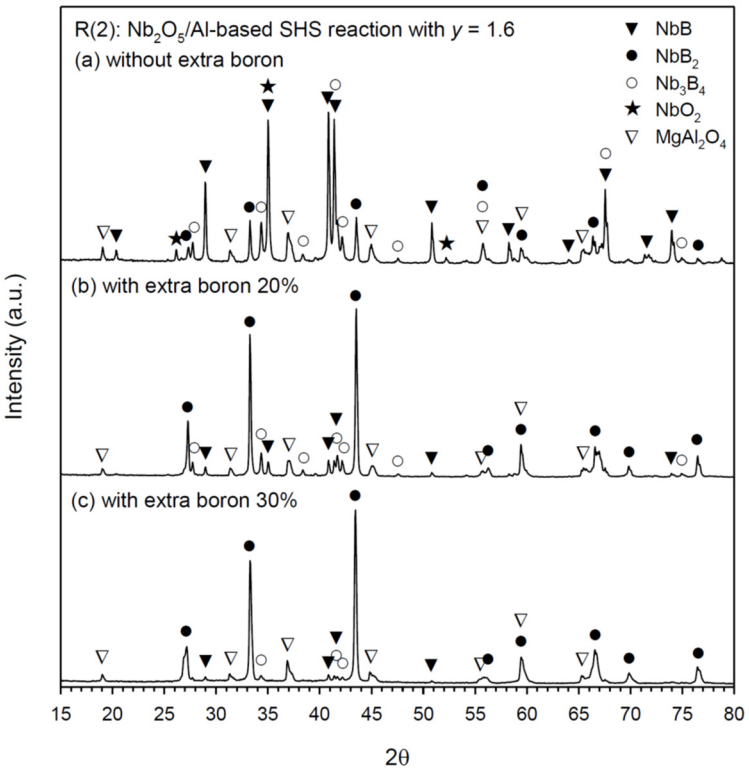

Figure 7. XRD patterns of NbB_2–$MgAl_2O_4$ composites synthesized from Reaction (2) of y = 1.6 under conditions: (**a**) without extra boron, (**b**) with extra boron 20%, and (**c**) with extra boron 30%.

Typical microstructures of the fracture surface of the NbB_2–$MgAl_2O_4$ composites synthesized from Reactions (1) and (2) with 30 atom.% extra boron are illustrated in Figure 8a,b, respectively.

As displayed in the micrographs of Figure 8a,b; the long rod-shaped $MgAl_2O_4$ crystals form a dense matrix with an interlocking structure and small NbB_2 grains are embedded in $MgAl_2O_4$ or distributed over the surface. Furthermore, $MgAl_2O_4$ and NbB_2 phases in Figure 8a are confirmed by the atomic ratios of Mg:Al:O = 14.1:28.9:57.0 and Nb:B = 32.7:67.3 deduced from the EDS spectrum. Similarly, in Figure 8b, $MgAl_2O_4$ and NbB_2 are determined to have Mg:Al:O = 13.7:29.8:56.5 and Nb:B = 33.1:66.9, both of which match well with their exact stoichiometries.

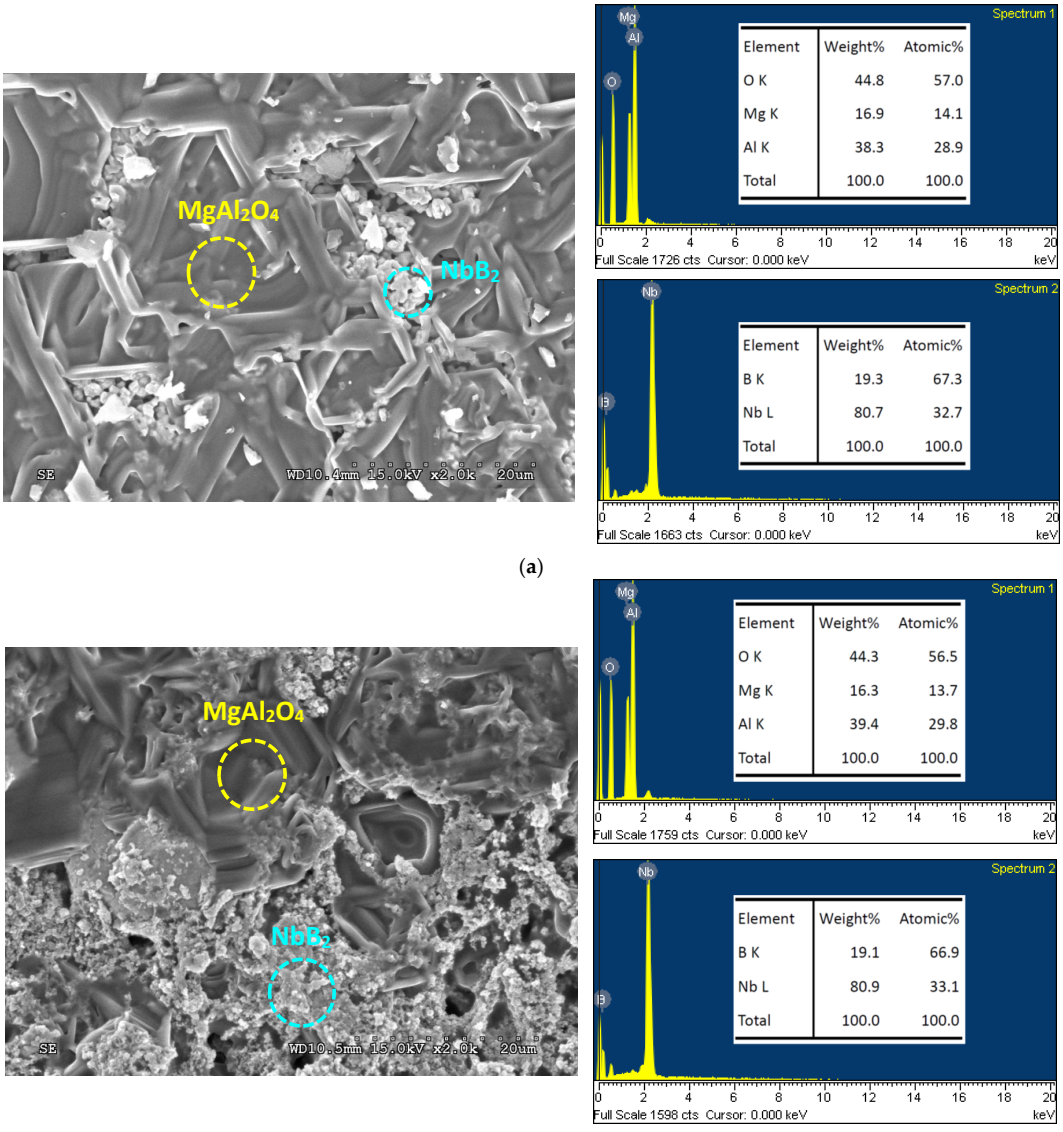

Figure 8. SEM micrographs and EDS spectra of NbB_2–$MgAl_2O_4$ composites of (**a**) Reaction (1) of $x = 1.0$ with 30 atom.% excess boron and (**b**) Reaction (2) of $y = 1.6$ with 30 atom.% excess boron.

Densified products have a relative density of about 92%–95%. For the NbB_2–$MgAl_2O_4$ composite synthesized from Reaction (1) of $x = 1.0$, $H_v = 15.2$ GPa and $K_{IC} = 4.82$ MPa $m^{1/2}$ were determined. The composite obtained from Reaction (2) of $y = 1.8$ exhibits $H_v = 16.9$ GPa and $K_{IC} = 4.37$ MPa $m^{1/2}$. When compared with pure NbB_2 ($K_{IC} = 3.76$ MPa $m^{1/2}$) [34], the NbB_2–$MgAl_2O_4$ composite is toughened. Similar materials like TiB_2–Al_2O_3 composites fabricated by hot pressing at a sintering temperature of 1700 °C showed a relative density of about 96.2%, Vickers hardness of 24.8 GPa, and fracture toughness of 4.56 MPa $m^{1/2}$ [35]. This confirms that satisfactory toughness is obtained for the NbB_2–$MgAl_2O_4$ composite synthesized by this study.

4. Conclusions

This study prepared NbB_2–$MgAl_2O_4$ in situ composites with a molar ratio of $NbB_2/MgAl_2O_4$ from 0.6 to 1.8 by the SHS process with reducing stages. Within the scope of experimental variables, combustion front velocity and temperature increased with NbB_2 content for Reaction (1), because the proportion of Nb_2O_5 to B_2O_3 in the thermite mixture increased. On the other hand, Reaction (2) showed a decrease in combustion velocity and temperature as NbB_2 content increased, because of the dilution effect of additional Nb and B on combustion. The activation energies, E_a = 219.5 ± 16 and 167.9 ± 13 kJ/mol, were, respectively, deduced for Reactions (1) and (2), suggesting a higher kinetic barrier for Reaction (1).

The XRD analysis of the final product confirms the formation of $MgAl_2O_4$ from thermite-produced Al_2O_3 and pre-added MgO. For the samples without extra boron, three boride phases, NbB, Nb_3B_4, and NbB_2, were formed and dominated by NbB. Excess boron up to 30 atom.% effectively compensated for the loss of boron during combustion and promoted the formation of NbB_2 as the major boride compound. The microstructure of as-synthesized NbB_2–$MgAl_2O_4$ composites is characterized by interlocking rod-shaped $MgAl_2O_4$ crystals and small NbB_2 grains embedded in $MgAl_2O_4$ or distributed over the surface. Fracture toughness of the NbB_2–$MgAl_2O_4$ composite was improved up to K_{IC} = 4.37–4.82 MPa $m^{1/2}$.

Author Contributions: Conceptualization, C.-L.Y. and Y.-C.C.; methodology, C.-L.Y. and Y.-C.C.; validation, C.-L.Y. and Y.-C.C.; formal analysis, C.-L.Y. and Y.-C.C.; investigation, C.-L.Y. and Y.-C.C.; resources, C.-L.Y.; data curation, C.-L.Y. and Y.-C.C.; writing—original draft preparation, C.-L.Y. and Y.-C.C.; writing—review and editing, C.-L.Y. and Y.-C.C.; supervision, C.-L.Y.; project administration, C.-L.Y.; funding acquisition, C.-L.Y. All authors have read and agreed to the published version of the manuscript.

Funding: This research work was funded by the Ministry of Science and Technology of Taiwan under the grant of MOST 108-2221-E-035-026.

Acknowledgments: Authors are thankful for Precision Instrument Support Center of Feng Chia University in providing materials analytical facilities.

Conflicts of Interest: The authors declare no conflicts of interest.

References

1. Okamoto, N.L.; Kusakari, M.; Tanaka, K.; Inui, H.; Otani, S. Anisotropic elastic constants and thermal expansivities in monocrystal CrB_2, TiB_2, and ZrB_2. *Acta Mater.* **2010**, *58*, 76–84. [CrossRef]
2. Kurbatkina, V.V.; Patsera, E.I.; Levashov, E.A.; Timofeev, A.N. Self-propagating high-temperature synthesis of refractory boride ceramics (Zr, Ta) B_2 with superior properties. *J. Eur. Ceram. Soc.* **2018**, *38*, 1118–1127. [CrossRef]
3. Alsawat, M.; Altalhi, T.; Alotaibi, N.F.; Zaki, Z.I. Titanium carbide—Titanium boride composites by self propagating high temperature synthesis approach: Influence of zirconia additives on the mechanical properties. *Results Phys.* **2019**, *13*, 102292. [CrossRef]
4. Demirskyi, D.; Vasylkiv, O. Mechanical properties of SiC–NbB_2 eutectic composites by in situ spark plasma sintering. *Ceram. Int.* **2016**, *42*, 19372–19385. [CrossRef]
5. Wuchina, E.; Opila, E.; Opeka, M.; Fahrenholtz, W.; Talmy, I. UHTCs: Ultra-high temperature ceramic materials for extreme environment applications. *Electrochem. Soc. Interface* **2007**, *16*, 30–36.
6. Yan, C.; Liu, R.; Zhang, C.; Cao, Y.; Long, X. A solid-state precursor route to MB_2–Al_2O_3 composite powders. *Powder Technol.* **2016**, *301*, 596–600. [CrossRef]
7. Mohammad Sharifi, E.; Karimzadeh, F.; Enayati, M.H. Synthesis of titanium diboride reinforced alumina matrix nanocomposite by mechanochemical reaction of Al–TiO_2–B_2O_3. *J. Alloy. Compd.* **2010**, *502*, 508–512. [CrossRef]
8. Xiao, G.Q.; Fu, Y.L.; Zhang, Z.W.; Hou, A.D. Mechanism and microstructural evolution of combustion synthesis of ZrB_2–Al_2O_3 composite powders. *Ceram. Int.* **2015**, *41*, 5790–5797. [CrossRef]
9. Yeh, C.L.; Chong, M.H. Effects of B4C and BN additions on formation of NbB_2–Al_2O_3 composites from reduction-based combustion synthesis. *Ceram. Int.* **2017**, *43*, 7560–7564. [CrossRef]

10. Yeh, C.L.; Huang, Y.S. Effects of excess boron on combustion synthesis of alumina-tantalum boride composites. *Ceram. Int.* **2014**, *40*, 2593–2598. [CrossRef]
11. Radishevskaya, N.; Lepakova, O.; Karakchieva, N.; Nazarova, A.; Afanasiev, N.; Godymchuk, A.; Gusev, A. Self-propagating high temperature synthesis of TiB_2–$MgAl_2O_4$ composites. *Metals* **2017**, *7*, 295. [CrossRef]
12. Ganesh, I. A review on magnesium aluminate ($MgAl_2O_4$) spinel: Synthesis, processing and applications. *Int. Mater. Rev.* **2013**, *58*, 63–112. [CrossRef]
13. Ma, Y.; Liu, X. Kinetics and thermodynamics of Mg-Al disorder in $MgAl_2O_4$-spinel: A review. *Molecules* **2019**, *24*, 1704. [CrossRef]
14. Mouyane, M.; Jaber, B.; Bendjemil, B.; Bernard, J.; Houivet, D.; Noudem, J.G. Sintering behavior of magnesium aluminate spinel $MgAl_2O_4$ synthesized by different methods. *Int. J. Appl. Ceram. Technol.* **2019**, *16*, 1138–1149. [CrossRef]
15. Padmaraj, O.; Venkateswarlu, M.; Satyanarayana, N. Structural, electrical and dielectric properties of spinel type $MgAl_2O_4$ nanocrystalline ceramic particles synthesized by the gel-combustion method. *Ceram. Int.* **2015**, *41*, 3178–3185. [CrossRef]
16. Zegadi, A.; Kolli, M.; Hamidouche, M.; Fantozzi, G. Transparent $MgAl_2O_4$ spinel fabricated by spark plasma sintering from commercial powders. *Ceram. Int.* **2018**, *44*, 18828–18835. [CrossRef]
17. Wen, Y.; Liu, X.; Chen, X.; Jia, Q.; Yu, R.; Ma, T. Effect of heat treatment conditions on the growth of $MgAl_2O_4$ nanoparticles obtained by sol-gel method. *Ceram. Int.* **2017**, *43*, 15246–15253. [CrossRef]
18. Lin, J.; He, Y.; Du, X.; Lin, Q.; Yang, H.; Shen, H. Structural and magnetic studies of Cr^{3+} substituted nickel ferrite nanomaterials prepared by sol-gel auto-combustion. *Crystals* **2018**, *8*, 384. [CrossRef]
19. Merzhanov, A.G. Combustion processes that synthesize materials. *J. Mater. Process. Technol.* **1996**, *56*, 222–241. [CrossRef]
20. Levashov, E.A.; Mukasyan, A.S.; Rogachev, A.S.; Shtansky, D.V. Self-propagating high-temperature synthesis of advanced materials and coatings. *Int. Mater. Rev.* **2017**, *62*, 203–239. [CrossRef]
21. Horvitz, D.; Gotman, I. Pressure-assisted SHS synthesis of $MgAl_2O_4$–TiAl in situ composites with interpenetrating networks. *Acta Mater.* **2002**, *50*, 1961–1971. [CrossRef]
22. Omran, J.G.; Afarani, M.S.; Sharifitabar, M. Fast synthesis of $MgAl_2O_4$–W and $MgAl_2O_4$–W–W2B composite powders by self-propagating high-temperature synthesis reactions. *Ceram. Int.* **2018**, *44*, 6508–6513. [CrossRef]
23. Zaki, Z.I.; Mostafa, N.Y.; Rashad, M.M. High pressure synthesis of magnesium aluminate composites with MoSi2 and Mo5Si3 in a self-sustaining manner. *Ceram. Int.* **2012**, *38*, 5231–5237. [CrossRef]
24. Yeh, C.L.; Chen, Y.C. Fabrication of MoSi2–$MgAl_2O_4$ in situ composites by combustion synthesis involving intermetallic and aluminothermic reactions. *Vacuum* **2019**, *167*, 207–213. [CrossRef]
25. Yeh, C.L.; Chen, Y.C. Formation of Mo_5Si_3/Mo_3Si–$MgAl_2O_4$ composites via self-propagating high-temperature synthesis. *Molecules* **2020**, *25*, 83. [CrossRef]
26. Cueilleron, J.; Thevenot, F. Chemical properties of boron. In *Boron and Refractory Borides*; Matkovich, V.I., Ed.; Springer: Berlin/Heidelberg, Germany, 1977; pp. 203–213.
27. Wang, L.L.; Munir, Z.A.; Maximov, Y.M. Thermite reactions: Their utilization in the synthesis and processing of materials. *J. Mater. Sci.* **1993**, *28*, 3693–3708. [CrossRef]
28. Yeh, C.L.; Ke, C.Y. Combustion synthesis of FeAl-based composites from thermitic and intermetallic reactions. *Crystals* **2019**, *9*, 127. [CrossRef]
29. Binnewies, M.; Milke, E. *Thermochemical Data of Elements and Compounds*; Wiley-VCH Verlag GmbH: Weinheim, NY, USA, 2002.
30. Liang, Y.H.; Wang, H.Y.; Yang, Y.F.; Zhao, R.Y.; Jiang, Q.C. Effect of Cu content on the reaction behaviors of self-propagating high-temperature synthesis in Cu-Ti-B_4C system. *J. Alloy. Compd.* **2008**, *462*, 113–118. [CrossRef]
31. Yeh, C.L.; Chen, Y.L. An experimental study on self-propagating high-temperature synthesis in the Ta-B_4C system. *J. Alloy. Compd.* **2009**, *478*, 163–167. [CrossRef]
32. Varma, A.; Rogachev, A.S.; Mukasyan, A.S.; Hwang, S. Combustion synthesis of advanced materials: Principals and applications. *Adv. Chem. Eng.* **1998**, *24*, 79–225.
33. Yeh, C.L.; Chen, W.H. A comparative study on combustion synthesis of Nb-B compounds. *J. Alloy. Compd.* **2006**, *422*, 78–85. [CrossRef]

34. Akin, I.; Ocak, B.C.; Sahin, F.; Goller, G. Effects of SiC and SiC-GNP additions on the mechanical properties and oxidation behavior of NbB_2. *J. Asian Ceram. Soc.* **2019**, *7*, 170–182. [CrossRef]
35. Liu, G.; Yan, D.; Zhang, J. Microstructure and mechanical properties of TiB_2–Al_2O_3 composites. *J. Wuhan Univ. Technol. Mater. Sci. Ed.* **2011**, *26*, 696–699. [CrossRef]